Geophysical Research Letters

Supporting Information for

Arctic amplification of global warming strengthened by sunlight oxidation of permafrost carbon to CO_2

J. C. Bowen[1], C. P. Ward[2], G. W. Kling[3], R. M. Cory[1]

[1]Department of Earth and Environmental Sciences, University of Michigan, Ann Arbor, MI, 48109. [2]Department of Marine Chemistry and Geochemistry, Woods Hole Oceanographic Institution, Woods Hole, MA, 02543. [3]Department of Ecology and Evolutionary Biology, University of Michigan, Ann Arbor, MI, 48109.

Joint corresponding authors: Collin Ward, cward@whoi.edu; Rose Cory, rmcory@umich.edu.

Contents of this file

Supporting Methods

1.1 Experimental design

Light exposure experiments were conducted to (i) characterize the spectral (wavelength) dependence of the photomineralization yield ($\varphi_{PM,\lambda}$) for permafrost dissolved organic carbon (DOC), (ii) quantify the radiocarbon (^{14}C) and stable carbon (^{13}C) isotopic compositions of carbon dioxide (CO_2) produced from photomineralization of permafrost DOC, and (iii) quantify changes in the chemical composition of permafrost DOC from light exposure. To test for controls on the $\varphi_{PM,\lambda}$ and the chemical composition of DOC photomineralized to CO_2, each light exposure experiment was conducted using DOC leached from five permafrost soils varying in DOC composition and iron concentration (Table S1, Figure S1; Ping et al., 1998; Trusiak et al., 2019). The study objectives required exposing permafrost DOC to different sources and doses of light. For objectives (i) and (ii), DOC from permafrost soils collected in 2018 were exposed to light using custom-built high-powered (≥ 100 mW), narrow-banded (± 10 nm) light-emitting diodes (LED). The $\varphi_{PM,\lambda}$ (objective (i)) was measured upon exposure of permafrost DOC to LEDs with peak emission at 278, 309, 348, 369, and 406 nm (Figure S1; see Methods). For objective (ii), the ^{14}C and ^{13}C compositions of dissolved inorganic carbon (DIC) in the permafrost leachates were measured upon exposure to LEDs at 309 and 406 nm alongside dark controls, and compared to the ^{14}C and ^{13}C compositions of DOC leached from the permafrost soil (Figure S1; see Methods). For objective (iii), we used permafrost soils collected in 2013 and 2015 from the same sites as in 2018 to quantify shifts in major functional groups of permafrost DOC by ^{13}C nuclear magnetic resonance (NMR) upon exposure to broadband light relative to dark controls (Figure S1). We also quantified $\varphi_{PM,\lambda}$ following the same exposure of these permafrost DOC samples to broadband light (Figure S1). Directly measured $\varphi_{PM,\lambda}$ spectra for permafrost DOC from objective (i) were used to calculate surface water rates of photomineralization as a function of increasing permafrost DOC in the DOC pool in surface waters.

1.2 Preparation and characterization of permafrost leachates from soils

Here we describe how permafrost leachates were prepared from soils collected in the summer of 2018 (Figure S1), including the precautions taken to minimize ^{14}C contamination during soil collection and while leaching DOC from those soils. We also describe the methodology for each chemical analysis conducted on the permafrost leachates prepared from soils collected in 2018.

1.2.1 Field and laboratory precautions to minimize ^{14}C contamination

Personnel digging soil pits and collecting soil samples wore new Tyvek protective coveralls (DuPont) and powder-free nitrile gloves (Kimberly-Clark) that were rinsed with deionized water (Barnstead E-Pure and B-Pure system) prior to soil collection. Soil samples were collected using a chisel that was rinsed with deionized water. Soil samples were quintuple-bagged using two Ziploc bags and three clear plastic bags so that a bag layer could be shed each time a sample was transferred to a new storage container (e.g., from a cooler to a freezer). Between shipments and experiments, soil samples were stored in freezers in ^{14}C-free facilities.

In the laboratory, the frozen soils were broken up into smaller pieces using a chisel that was rinsed with MilliQ water (Millipore Simplicity ultraviolet, UV, system) in between each use. New 5 gallon high-density polyethylene (HDPE) buckets with lids (Uline, Inc.) were used to leach the permafrost DOC. Those buckets were cleaned in between each use by rinsing 30 times with MilliQ water, soaking overnight in MilliQ water, and then rinsing again 30 times with MilliQ water. Each permafrost leachate was filtered through a sieve that was rinsed 30 times with MilliQ water in between use, and through new, MilliQ-rinsed high-capacity cartridge filters.

A leach test was conducted to quantify potential DOC contamination from the HDPE buckets by filling two HDPE buckets with five liters of MilliQ water covered with a HDPE lid. Buckets were leached at 25 °C for 24 hours. DOC was analyzed on the initial MilliQ water added to the buckets and on

the water in each bucket after 24 hours using a Shimadzu TOC-V analyzer. The HDPE buckets leached on average 4.8 ± 2.2 μM DOC into solution during the 24-hour leaching (± 1 standard error, SE; n = 2; leaching rate of 58 ± 26 μg DOC L^{-1} per day). If each permafrost leachate was in a HDPE bucket for 2 days, and the DOC leached from plastic buckets were fossil (i.e., $\Delta^{14}C$ = -1000‰), then DOC leached from the HDPE buckets would result in ^{14}C-depletion of the permafrost DOC by -3.6 ± 1.1‰ (± 1 SE; n = 5 permafrost leachates). Thus, any ^{14}C contamination from using the 5 gallon HDPE buckets to leach DOC from the permafrost soil was within the instrumental precision of the radiocarbon analyses (≤ 6‰; see Methods).

1.2.2 Permafrost soil collection

Soil cores were collected at Imnavait wet sedge tundra using a SIPRE corer, and the permafrost layer (1.0 – 1.3 m below the surface) was separated from the soil core using a knife (Table S1). At the other four sites, 1 m x 1 m x 1 m soil pits were excavated using a jack hammer, shovels, and pickaxe (Table S1). Soil sampling at each site took place over the course of one day. From each site, an equal mass of soil (~2.5 kg) was placed in four Ziploc bags (1 gallon) and then each soil sample was quintuple-bagged. Following collection, soil samples were immediately transferred to coolers in the field and then stored in freezers at the Toolik Lake Field Station for ≤ 4 weeks until overnight shipment on dry ice to the Woods Hole Oceanographic Institution (WHOI). All soil samples were frozen upon arrival at WHOI and immediately placed into ^{14}C-free freezers until further use.

1.2.3 Permafrost leachate preparation and characterization

DOC was leached from each permafrost soil at WHOI as described in the following five steps. First, frozen soil in one or two Ziploc bags was broken into smaller pieces inside the bag using a clean chisel. Second, 0.8 to 3.3 kg of frozen soil was transferred to a new Ziploc bag (1 gallon) and then thawed in a chest cooler at 4 °C for up to 20 hours (Table S6). Third, the thawed permafrost soil was added to five liters of MilliQ water in a MilliQ-rinsed HDPE bucket (5 gallon). Each bucket was covered with a HDPE lid and allowed to leach at 4 °C for 24 hours. Fourth, the permafrost leachate was filtered through a sieve with 60 μm nylon mesh screening (Component Supply) into a new, MilliQ-rinsed 5 gallon HDPE bucket and then placed in the chest cooler at 4 °C for ≤ 1 day to allow suspended particles to settle before additional filtration. Fifth, the 60-μm filtered leachate was filtered through 10 μm (Geotech Environmental Equipment, Inc.) and then finally through 0.2 μm (Whatman), MilliQ-rinsed high-capacity cartridge filters. Four liters of the final 0.2-μm filtered permafrost leachate (now referred to as permafrost leachate) were then transferred to a precombusted (450 °C; 4 h) 4 L glass amber bottle and kept at 4 °C prior to ^{14}C and ^{13}C analyses and the light exposure experiments. The remaining one liter of the permafrost leachate was transferred to amber HDPE bottles for water chemistry analyses (excluding ^{14}C and ^{13}C analyses).

Water chemistry analyses (pH, specific conductivity, iron, DOC, and cations) were performed on each of the permafrost leachates, as previously described (Kling et al., 2000; Cory et al., 2013). Dissolved total and reduced iron concentrations were quantified using the Ferrozine method (Stookey, 1970) immediately after permafrost leachate preparation (detection limit = 1 μM; coefficient of variance, CV, < 2% on triplicate analyses; Cory et al., 2015). DOC concentrations were measured using a Shimadzu TOC-V analyzer (CV < 5% on duplicate analyses; Kling et al., 2000). Water samples were analyzed for cations on a Thermo Scientific 2 High-Resolution inductively coupled plasma mass spectrometer (ICP-MS; CV < 2% on triplicate analyses; Linge & Jarvis, 2009). Chromophoric and fluorescent dissolved organic matter (CDOM and FDOM, respectively) were measured for each permafrost leachate (Cory et al., 2014), and then the spectral slope ratio (S_R), specific UV absorbance at 254 nm ($SUVA_{254}$), and fluorescence index were calculated as previously described (Cory et al., 2014).

1.3 Photon fluxes and rates of light absorption during LED experiments to characterize apparent quantum yield spectra

Solar irradiance spectra were measured from each ≥ 100 mW, narrow-banded (± 10 nm) LED (LG Innotek 6060 Series) at 278, 309, 348, 369, and 406 nm. The solar irradiance spectrum (W m^{-2} nm^{-1}) was measured in triplicate at the same height as the flat bottom of the 12 mL quartz vial and in each of the four positions of the inner aluminum housing with a radiometer over wavelengths from 250 to 500 nm (NIST-Calibrated Black Comet Spectral Radiometer, StellarNet, Inc.). Each spectrum (W m^{-2} nm^{-1}) was converted to a photon flux spectrum (mol photon m^{-2} s^{-1} nm^{-1}). The total photon flux spectrum during the light exposure period ($E_{0,\lambda}$; mol photon m^{-2} nm^{-1}) was calculated as the average of triplicate measurements multiplied by the light exposure time. The photon dose was calculated as the sum of the total photon flux spectrum across all wavelengths (mol photon m^{-2}).

A cross-validation of the photon flux estimated by radiometry was conducted using nitrite actinometry (Jankowski et al., 1999). There was a < 10% difference in the photon flux of the 348-nm LED determined by actinometry versus radiometry (described above). Thus, the photon flux spectra from radiometry measurements were used to calculate the amount of light absorbed by CDOM in the quartz vials during each light exposure period.

For each vial exposed to a LED, the amount of light absorbed by CDOM ($Q_{a\lambda}$; mol photons m^{-2}) was calculated following:

$$Q_{a,\lambda} = \int_{\lambda_{min}}^{\lambda_{max}} E_{0,\lambda}(1 - e^{-a_{CDOM,\lambda} * z}) \frac{a_{CDOM,\lambda}}{a_{tot,\lambda}} d\lambda \quad (1)$$

where λ_{min} and λ_{max} are the minimum and maximum wavelengths of light absorbed by CDOM and $E_{0,\lambda}$ is the total photon flux spectrum reaching the quartz vial from an LED during the light exposure period (± 10 nm; n = 3; mol photon m^{-2} nm^{-1}). $a_{CDOM,\lambda}$ was calculated as the geometric mean of the light-exposed and dark control absorption coefficients of CDOM to account for loss of light-absorbing DOC (i.e., photobleaching of CDOM) during the light exposure period. We assumed that the pathlength (z) was equivalent to the height of each quartz vial (10 cm) and that $a_{CDOM,\lambda}/a_{tot,\lambda}$ was equal to 1 given that CDOM was the main constituent absorbing light at UV and visible wavelengths in the filtered permafrost leachates (Cory et al., 2014). The amount of light absorbed by CDOM at each wavelength was calculated as the average ± 1 SE of experimental replicate vials (n = 4). There was < 5% CV in the amount of light absorbed by CDOM between the experimental replicate vials (n = 4).

The irradiances received by permafrost DOC were chosen to achieve similar amounts of light absorbed by CDOM during the light exposure period at each wavelength and between all permafrost leachates. Thus, irradiances were chosen by taking into account that concentrations of a_{CDOM} decrease with increasing wavelength and permafrost leachates had different a_{CDOM} concentrations (Table S6). Photon doses ranged from 2 mol photon m^{-2} at 278 nm to 6 mol photon m^{-2} at 406 nm, resulting in an average of 2.40 ± 0.04 mol photon m^{-2} of light absorbed by CDOM at all wavelengths for four of the five permafrost leachates (± 1 SE; n = 20). The exception was the Sagwon moist acidic tundra permafrost leachate, which had no detectable CO_2 production at any wavelengths after CDOM absorbed 2.40 ± 0.04 mol photon m^{-2} of light. Thus, the Sagwon moist acidic tundra permafrost leachate was exposed to the LEDs for 30 hours with photon doses ranging from 5 to 28 mol photon m^{-2}, which resulted in an average of 4.04 ± 0.22 mol photon m^{-2} of light absorbed by CDOM at all wavelengths (± 1 SE; n = 5). The photon doses received by each permafrost leachate and amounts of light absorbed by CDOM in each permafrost leachate during LED exposure at 309 nm are reported in Table S3.

1.4 Photomineralization rate calculations

First, to quantify the effect of the shallower slope of the $\varphi_{PM,\lambda}$ spectrum on photomineralization rates, we calculated photomineralization rates in Imnavait Creek using the average $\varphi_{PM,\lambda}$ spectrum of the DOC in this surface water (Cory et al., 2014, 2015; Figure S5) versus the $\varphi_{PM,\lambda}$ spectrum of Imnavait moist acidic tundra permafrost DOC (Figure 1a). Water column rates of photomineralization (mmol C m^{-}

^{2} d^{-1} nm^{-1}) were calculated in Imnavait Creek as the product of two spectra: the rate of light absorption by CDOM throughout the water column ($Q_{a,\lambda}$; mol photon m^{-2} d^{-1} nm^{-1}) and the apparent quantum yield for photomineralization ($\varphi_{PM,\lambda}$; mmol C mol photon^{-1} nm^{-1}):

$$\text{Rate of DOC photomineralization} = \int_{\lambda_{min}}^{\lambda_{max}} Q_{a,\lambda}\varphi_{PM,\lambda}\, d\lambda \quad (2)$$

Water column rates of light absorption by CDOM were calculated using the average $a_{CDOM,\lambda}$ in Imnavait Creek (m^{-1}; Cory et al., 2014, 2015), the average depth of Imnavait Creek (0.5 m), and the daily incoming photon flux spectrum (mol photon m^{-2} d^{-1} nm^{-1}) measured on 21 June 2018 at the nearby Toolik Lake Field Station. Thus, differences in water column rates of photomineralization were due only to the $\varphi_{PM,\lambda}$ spectrum (Figure 3a).

Second, to estimate the effect of permafrost DOC on photomineralization rates in arctic surface waters, we quantified photomineralization rates in Imnavait Creek, Kuparuk River, and Toolik Lake (representative surface waters in the Arctic; Cory et al., 2014) if permafrost DOC made up 0, 5, 10, 15, 20, and 25% of the total DOC pool. Photomineralization rates were estimated by 'mixing' (in the stated proportions of 0-25%) the $\varphi_{PM,\lambda}$ spectra for each of the five permafrost DOC samples in this study (Figure 1a) with the $\varphi_{PM,\lambda}$ spectra for DOC in each of the three surface waters (Cory et al., 2014; Figure S5). For each calculation, a 'mixed' $\varphi_{PM,\lambda}$ spectrum was generated using a mixing equation ($\varphi_{PM\text{-}mixture,\lambda}$), where X is the fraction of permafrost DOC comprising the DOC pool (0-25%):

$$\varphi_{PM\text{-}mixture,\lambda} = (\varphi_{PM\text{-}permafrost,\lambda} * X) + (\varphi_{PM\text{-}surface\ water,\lambda} * (1 - X)) \quad (3)$$

Water column rates of photomineralization (mmol C m^{-2} d^{-1} nm^{-1}) were calculated as described above in the example for Imnavait Creek using the respective water column depth and average $a_{CDOM,\lambda}$ for each surface water (Cory et al., 2014, 2015), and the daily incoming photon flux spectrum measured on 21 June 2018 at the Toolik Lake Field Station; described below). There were 90 photomineralization rates calculated: 5 permafrost $\varphi_{PM,\lambda}$ spectra x 3 surface water $\varphi_{PM,\lambda}$ spectra x 6 fractions of permafrost DOC in the DOC pool. The percent change in water column rates of photomineralization relative to no permafrost DOC is shown for each surface water DOC in Figure 3b as the average ± 1 SE of the calculated rates (n = 5 for each fraction of permafrost DOC in the DOC pool). The percent change in water column rates of photomineralization relative to no permafrost DOC in the surface water DOC pool is reported in the main text as the average ± 1 SE of the calculated rates in all three surface waters (n = 15 for each fraction of permafrost DOC in the DOC pool). The variance of each estimate represents the difference in the magnitude of the photomineralization yield spectra between each permafrost DOC and the DOC from each of three arctic surface waters (Cory et al., 2014). When reporting the results of these calculations, we assumed that all controls on DOC photomineralization aside from the $\varphi_{PM,\lambda}$ spectrum remain the same as previously described; i.e., DOC photomineralization will remain light-limited (Cory et al., 2015) and independent of rates of water column mixing (Li et al., 2019), and that any DOC photomineralized to CO_2 is rapidly replenished by new DOC exported from the riparian zone (Merck et al., 2012; Neilson et al., 2018).

1.5 Daily photon flux spectra reaching the Toolik Lake Field Station

Daily downward photon flux spectra were generated from 15 May to 1 Oct for 2012, 2015, 2016, 2017, and 2018 as previously described (Cory et al., 2014). Briefly, direct measurements of UV and photosynthetically active radiation (PAR) at the Toolik Lake Field Station (68.62° N, 149.29° W) were apportioned to a modeled solar spectrum and separated into direct and diffuse spectra. Wavelength-dependent correction factors were then applied to those spectra to account for atmospheric turbidity and Rayleigh scattering. The global photon flux spectra (mol photon m^{-2} s^{-1} nm^{-1}) were calculated as the sum

of the corrected direct and diffuse photon flux spectra multiplied by the duration of time between consecutive UV and PAR measurements (5 minutes and hourly, respectively). Daily downward photon flux spectra were calculated as the sum of photon flux spectra for each time interval during each day (mol photon m^{-2} d^{-1} nm^{-1}).

Daily photon flux spectra were summed from 280 to 400 nm and 401 to 700 nm to calculate daily UV and PAR photon doses, respectively. Total summertime UV and PAR photon doses were then calculated as the sum of daily UV and PAR photon doses from 15 May to 1 Oct for each year (Table S5). There was on average 11-fold more visible light than UV light reaching the Toolik Lake Field Station for the 2012, 2015, 2016, and 2017 summer seasons (Table S5).

1.6 Photochemical changes in DOC composition

Permafrost soils collected in 2013 and 2015 were used to evaluate changes in DOC chemical composition by ^{13}C-NMR following light exposure and to quantify $\varphi_{PM,\lambda}$ (Figure S1). Sampling and preparation of the permafrost leachates from soils collected in 2013 and 2015 were previously described (Ward & Cory, 2015; Ward et al., 2017) and similar to the methods described above for soils collected in 2018. All information on samples collected in 2013 were previously published (Ward & Cory, 2015). Here we describe methods used in this study to quantify photochemical changes in DOC chemical composition and the $\varphi_{PM,\lambda}$ for DOC leached from permafrost soils collected in 2015.

Each permafrost leachate was exposed to 18 hours of simulated sunlight at 20 °C (Atlas Suntest XLS+) in Whirl-Pak bags (Nasco, Inc.) alongside dark controls (Figure S1). Dissolved organic matter in the light-exposed and dark control waters was isolated by solid-phase extraction, freeze-dried, and analyzed by solid-state ^{13}C-NMR as previously described (Ward & Cory, 2015, 2016). The percentages of aromatic and carboxyl C within the DOC pool (Cory et al., 2007) are reported as the average ± 1 SE of the experimental replicate leachates (n = 2), except for Toolik moist acidic tundra, which did not have an experimental replicate (Table S7). The percent loss of carboxyl C was calculated as previously described (Ward & Cory, 2016) and reported as the average ± 1 SE of the experimental replicate leachates (n = 2; Figure S2).

From these same broadband light exposure experiments used to determine changes in DOC composition by ^{13}C-NMR, we determined $\varphi_{PM,\lambda}$ by measuring DIC and CDOM in triplicate gas-tight, precombusted 12 mL borosilicate exetainer vials (450 °C; 4 hrs; Labco, Inc.) alongside dark controls (Table S3, Figure S1; Cory et al., 2014). The solar irradiance spectrum (W m^{-2} nm^{-1}) was measured in duplicate at the surface of the Suntest XLS+ with a radiometer over wavelengths from 280 to 700 nm (USB4000 Spectrometer, Ocean Optics). The amount of light absorbed by CDOM (mol photon m^{-2} nm^{-1}) was calculated as previously described (Cory et al., 2014). $\varphi_{PM,\lambda}$ was calculated as the light minus dark difference in DIC concentration divided by the light absorbed by CDOM during the light exposure period, assuming the $\varphi_{PM,\lambda}$ spectrum decreased exponentially with increasing wavelength (Cory et al., 2014). The $\varphi_{PM,\lambda}$ for each permafrost leachate is reported as the average ± 1 SE of replicate experiments (n = 2; Figure 1b), except for Toolik moist acidic tundra, which only had one experiment conducted.

1.7 Statistical analyses

Statistical tests were used to determine whether light exposure of permafrost DOC resulted in significant changes in DOC concentration and chemical composition, and whether light minus dark differences in DOC concentration and chemical composition changed significantly as a function of light wavelength or dissolved iron concentration. Two-tailed, paired t-tests were conducted to determine significant differences in DIC concentrations, dissolved oxygen (O_2) concentrations, Δ^{14}C and δ^{13}C of DIC, and percentages of carboxyl C within DOC in the light-exposed versus dark control leachates. Statistical significance was defined as $p < 0.05$. T-tests were used to determine whether the slopes and intercepts of each regression in Figures 1, 2, S2, S4, and S6 were significantly different from zero. T-tests were used to determine whether the slopes and intercepts of least-squares regressions between cation, DOC composition, or $\varphi_{PM,\lambda}$ data were significantly different from zero (see Supporting Text). The

open symbols for Toolik moist acidic tundra permafrost DOC in Figures 1b and S2 were identified as outliers because the value for this permafrost DOC was more than ± 5 standard deviations from the slope of the least-squares regression (see Supporting Text).

Statistical analyses were conducted to determine whether the $\varphi_{PM,\lambda}$ and $\varphi_{PO,\lambda}$ spectral slopes of permafrost and surface water DOC were significantly different from one another. Two-tailed, unpaired t-tests or analysis of variance were used to determine significant differences between the slopes of the $\varphi_{PM,\lambda}$ or $\varphi_{PO,\lambda}$ spectra among permafrost DOC in Figures 1a or S6, and between permafrost and surface water DOC in Figures 1a and S5.

Supporting Text

2.1 Total dissolved iron concentrations

There was a significant, positive linear relationship between the total dissolved iron concentration quantified using the Ferrozine method (Stookey, 1970) versus by ICP-MS (Linge & Jarvis, 2009) for permafrost leachates prepared from soils collected in 2018 (t-statistic = 57.4, $p < 0.001$; Table S6). Because the Ferrozine method was used to quantify total dissolved iron in all permafrost leachates in this study (prepared from soils collected in 2013, 2015, and 2018), we report the results from this method in Figures 1b and S2.

2.2 Lability of permafrost DOC to photomineralization

There were significant, positive linear relationships between the $\varphi_{PM,\lambda}$ for permafrost DOC at 278, 309, 348, and 406 nm (in Figure 1a) versus the total dissolved iron concentration in permafrost leachates prior to light exposure ($p < 0.05$; quantified either using the Ferrozine method or by ICP-MS; Stookey, 1970; Linge & Jarvis, 2009). In contrast, there were no significant correlations of the $\varphi_{PM,\lambda}$ at any wavelength (Figure 1a) with concentrations of other dissolved cations in the permafrost leachates (Na, Ca, K, Mg, Ba, Mn, Zn, Al, or Si as quantified by ICP-MS; Table S6; Linge & Jarvis, 2009). There were no significant correlations of the $\varphi_{PM,\lambda}$ at any wavelength (Figure 1a) with any proxy for the aromatic content of DOC (e.g., a_{305}, $SUVA_{254}$, or the fluorescence index) or a proxy for the average molecular weight of DOC (S_R; Table S6).

Photomineralization yields at 309 nm ($\varphi_{PM,309}$) for permafrost DOC exposed to either broadband light or a ≥ 100 mW, narrow-banded (± 10 nm) LED were significantly, positively correlated with total dissolved iron concentration in the permafrost leachates prior to light exposure (t-statistic = 8.2 or 5.0, respectively; $p < 0.05$; Figure 1b). There were no significant correlations of these $\varphi_{PM,309}$ values (Figure 1b) with any proxy for DOC chemical composition, such as a_{305}, $SUVA_{254}$, S_R, or fluorescence index (Tables S6, S7). There were no significant correlations of $\varphi_{PM,309}$ obtained from exposure of permafrost DOC to broadband light (Figure 1b) with the % of aromatic or carboxyl C in the initial permafrost DOC quantified by ^{13}C-NMR (Table S7).

The Toolik moist acidic tundra permafrost leachate that was exposed to broadband light (Figure S1) was an outlier in the relationships shown in Figures 1b and S2. In Figure 1b, Toolik moist acidic tundra permafrost DOC showed a significantly lower $\varphi_{PM,309}$ than expected based on the initial iron concentration in the leachate (open red symbol). A lower photomineralization yield than expected may be due to the 2.6-fold higher light absorption of this permafrost DOC compared to the average amount of light absorbed by CDOM in the other permafrost leachates shown in Figure 1b (Table S3). As photon dose increases, the most photo-labile components of the DOC pool are consumed or altered, leaving behind less labile moieties with a lower capacity to form CO_2 per mol photon absorbed by DOC (Miller & Zepp, 1995). It is likely that most of the CO_2 was produced from Toolik moist acidic tundra permafrost DOC after relatively less light was absorbed by CDOM (i.e., after a shorter light exposure time). As CDOM continued to absorb light over the course of the experiment, less and less CO_2 was produced. Assuming that was the case, then $\varphi_{PM,309}$ is lower than expected based on the amount of iron present

initially because it was calculated as the amount of CO_2 produced divided by more photons than were needed to produce that CO_2.

The relatively higher amount of light absorbed by CDOM in the Toolik moist acidic tundra permafrost leachate (Table S3) is consistent with this permafrost DOC as an outlier in Figure S2, showing no detectable loss of carboxyl C despite having the highest total dissolved iron concentration. Photodegradation of DOC is thought to both produce and remove carboxyl C (Xie et al., 2004). Thus, no detectable loss of carboxyl C after exposure to a relatively higher photon dose compared to the other permafrost DOC samples may be due to concurrent photochemical production and loss of carboxyl C, such that production of carboxyl C masks the loss of labile carboxyl C from photo-decarboxylation (Xie et al., 2004).

Photomineralization rates averaged across all sites (lake and river) increased by 7 ± 3% (10% permafrost DOC addition) to 52 ± 20% (75% permafrost DOC addition, compared to no permafrost DOC in the DOC pool; ± 1 SE; n = 15; Figure 3b). For only lakes, the photomineralization rates increased by 94.5 ± 45% at 75% permafrost DOC addition (average ± 1 SE; n = 5; Figure 3b). The increase in photomineralization rates as permafrost DOC is exported to surface waters is due to significantly shallower spectral slopes directly measured in this study using LEDs compared to those quantified indirectly for arctic surface water DOC (two-tailed, unpaired t-test; $p < 0.001$; Figure S5). A shallower spectral slope for permafrost compared to surface water DOC indicates relatively lower lability to photomineralization at UV wavelengths and higher lability at visible wavelengths (different at 95% confidence interval; Figure S5). For example, higher lability of Imnavait moist acidic tundra permafrost DOC at visible wavelengths increased photomineralization rates in sunlit waters by nearly two-fold (6 ± 0.7 mmol CO_2 m^{-2} d^{-1} for Imnavait Creek DOC versus 10 ± 0.1 mmol CO_2 m^{-2} d^{-1} for Imnavait moist acidic tundra permafrost DOC; average ± 1 SE; n = 5 and 4, respectively; Figure 3a).

2.3 Photochemical production of ^{13}C-depleted CO_2

Photochemical production of ^{13}C-depleted CO_2 (Figure S4) was interpreted as the preferential photomineralization of DOC compounds that were ^{13}C-depleted. An alternative explanation is that photochemical isotope fractionation is taking place and resulting in an offset of the $\delta^{13}C$ of CO_2 relative to the $\delta^{13}C$ of initial DOC. Such fractionation has been reported for organic pollutants (Ratti et al., 2015; Willach et al., 2018), but not for DOC. However, there is no current method to our knowledge to determine the effect of $\delta^{13}C$ source versus fractionation on the net offset of the $\delta^{13}C$ of CO_2 relative to the $\delta^{13}C$ of initial DOC. Given that lignin and tannin are commonly more depleted in ^{13}C compared to other fractions of DOC (Benner et al., 1987; Bertoldi et al., 2014), and lignin and tannin are preferentially removed during light exposure of permafrost DOC (Ward & Cory, 2016; Ward et al., 2017), the most robust and simple interpretation is that ^{13}C-depleted DOC is photomineralized.

Together our results strongly suggest that iron catalyzes the oxidation of carboxylic acids attached to organic matter derived from lignin and tannin (Figures 1b, S2, S3, and S4). Given the evidence for iron-catalyzed photo-decarboxylation, we suggest that iron was likely closely associated (i.e., complexed) with the carboxylic acids that were photomineralized to CO_2 (Fujii et al., 2014).

2.4 Comparative photochemical strengthening of arctic amplification

Determining the relative importance of photochemical conversion of permafrost C to CO_2 compared to net ecosystem storage (gain or loss) of C depends in part on the variability of model-predicted storage. As the net ecosystem storage term approaches zero, the photochemical term, which is always a loss of C to the atmosphere, will increase in importance. This is analogous to the current situation for the arctic terrestrial C balance, where aquatic losses of CO_2 to the atmosphere can be ~40-100% of net ecosystem exchange depending on the net terrestrial balance in any one year (Kling et al., 1991; McGuire et al., 2009). That is, for either the current arctic C balance or predicted C balance given permafrost degradation, if the estimated or predicted net ecosystem C storage is zero then up to 100% of C loss to the atmosphere comes from photomineralization in surface waters. To estimate the probability

that model predictions in McGuire et al. (2018) fell within any given range, say -100 to +100 Pg C storage, we fit the data from McGuire et al. Figure 3 to a normal distribution. This fitting included results from all five models used at both scenarios (RCP4.5 and RCP8.5) and both time points (2100 and 2299). For the RCP8.5 scenario at 2299, there was a cumulative probability of 0.40 (40%) that the average model predictions fell between -200 (loss to atm) to +200 Pg C (gain to land), and a 20% probability that the model predictions fell between -100 to +100 Pg C. The probabilities (percentages) that all other combinations of scenarios and time points (RCP4.5, RCP8.5, 2100, 2299) had model predictions between -100 to +100 Pg C ranged from 57% to 74%.

DOC from permafrost is more labile to photomineralization than DOC from currently thawed soils (Figures 3a, S5; Section 2.2 above). We calculated the impact of this lability on future rates of photomineralization assuming that from 2010 to 2299 75% of the DOC in surface waters was leached from thawed permafrost soils (Figure 3b), and we used the area of permafrost lost by 2299 in the RCP8.5 scenario from McGuire et al. (2018). For this area of permafrost lost we assumed a surface water fraction of 6% (Cooley et al., 2019; S. Cooley, X. Yang, T. Pavelsky personal communication). We used a rate of surface water photomineralization corresponding to the Toolik Lake value when 75% of the DOC is from permafrost of 39 g C m^{-2} y^{-1}, which is 94.5% higher (Figure 3b) than the 20 g C m^{-2} y^{-1} photomineralization reported in Cory et al. (2014). This rate applied to the area of surface water in the area thawed by permafrost results in ~9 Pg C photomineralized to CO_2.

As described in Plaza et al. (2019), potentially more than half of the C loss from thawing permafrost soils could be in lateral water flow rather than directly to the atmosphere. That means of the 208 Pg C predicted average ecosystem loss from thawing permafrost by 2299 (RCP8.5; McGuire et al., 2018), another ~100 Pg C may move from thawing permafrost soils to surface waters. We assume that this 100 Pg C exported from permafrost soils to surface waters in headwater catchments is primarily DOC (Judd & Kling, 2002; Kling et al., 2014). To calculate the amount of this C that could be photomineralized, we used the ratio of DOC exported from the Kuparuk River basin each year (McGuire et al., 2009) to the photomineralization of DOC in the Kuparuk basin per year (Cory et al., 2014). This ratio shows that ~ 11% of the C moved from land to surface waters would be photomineralized using the photomineralization rate of 20 g C m^{-2} y^{-1}, and if the higher rate for permafrost DOC of 39 g C m^{-2} y^{-1} is used, then ~ 21% or 21 Pg of the 100 Pg C from land could be mineralized in surface waters. Combining the photomineralization of ~ 9 Pg C with the additional photomineralization of 21 Pg C from the lateral loss of C gives a value of 30 Pg C from photomineralization, or ~14% of the 208 Pg C lost from permafrost by 2299 (McGuire et al., 2018).

These predictions are likely conservative for several reasons. First, we are not including the photo-stimulated respiration of bacteria that is at least an additional 20% CO_2 produced in surface waters (Cory et al., 2013, 2014). Second, we are using ecosystem C losses and not soil C losses (which are higher; McGuire et al., 2018) to estimate the lateral hydrologic loss. Third, we are not considering the photodegradation of permafrost-derived DOC and particulate organic carbon laterally transported to surface waters during thermo-erosional failures (Cory et al., 2013; Turetsky et al., 2019). Fourth, we are not accounting for earlier ice-off on lakes that would increase the time of open water and thus the annual surface water photomineralization of DOC (Šmejkalová et al., 2016). Finally, we are not accounting for any photomineralization once river DOC enters oceans.

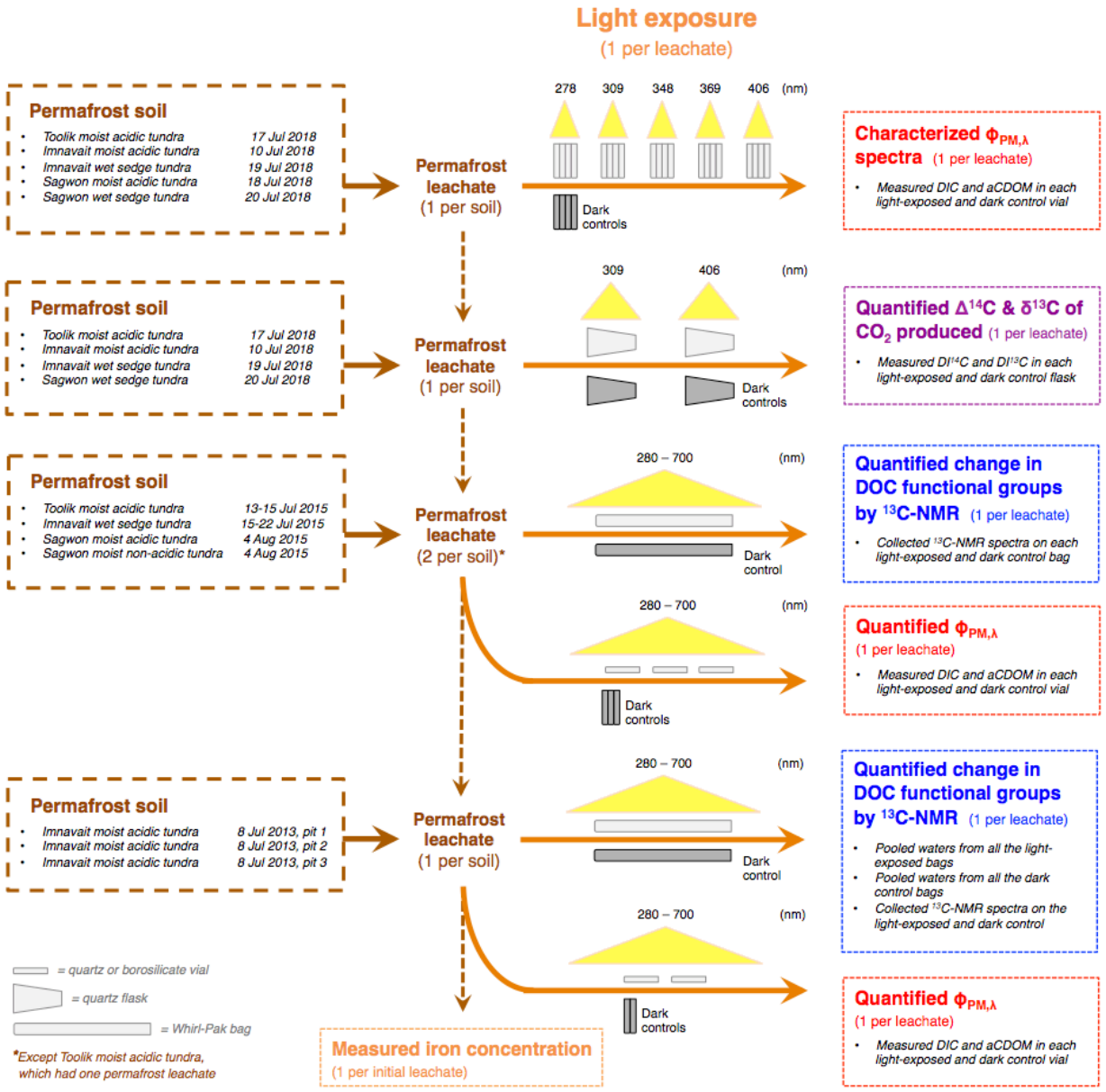

Figure S1. Experimental design for the light exposure experiments of permafrost DOC. Permafrost soils were collected at six different sites from two dominant vegetation types of the low Arctic and three glacial surfaces (Mull & Adams, 1989; Walker et al., 2005; Hobbie & Kling, 2014) on the dates indicated in the figure. One or two permafrost leachates were prepared from each permafrost soil. The concentration of total dissolved iron was measured in each permafrost leachate prior to light exposure following Stookey (1970). Each permafrost leachate was exposed to either high-powered (≥ 100 mW), narrow-banded (± 10 nm) LEDs (at 278, 309, 348, 369, or 406 nm) or broadband light (280 – 700 nm; Tables S3, S4). Details from the light exposure of DOC leached from Imnavait moist acidic tundra permafrost soil collected in 2013 were previously reported (Ward & Cory, 2016).

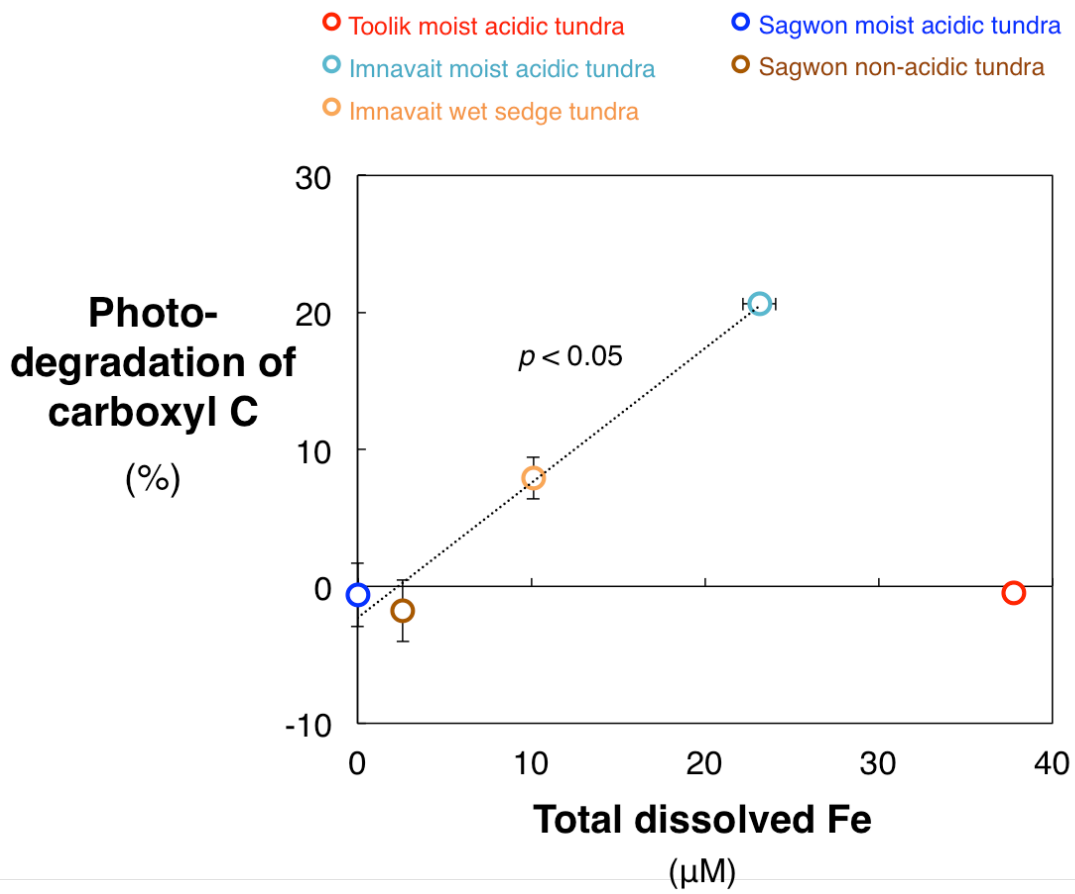

Figure S2. Photochemical degradation of carboxyl C increased with increasing dissolved iron. Percentage of carboxyl C degraded after exposure of permafrost DOC to broadband light relative to dark controls (quantified by ^{13}C-NMR) versus the total dissolved iron concentration in permafrost leachates prior to light exposure. Data were fit using a least-squares regression where $R^2 = 0.98$, t-statistic = 9.4, $p < 0.05$, excluding the red symbol (see Supporting Text). Data for Imnavait moist acidic tundra permafrost DOC were previously reported (Ward & Cory, 2016). All values on the x-axis are shown as the average ± 1 standard error of replicate permafrost leachates ($n = 2$, except Imnavait moist acidic tundra, which had $n = 3$). All values on the y-axis are shown as the average ± 1 standard error of replicate experiments ($n = 2$), except Toolik moist acidic tundra and Imnavait moist acidic tundra, which only had one experiment conducted (see Supporting Methods; Ward & Cory, 2016).

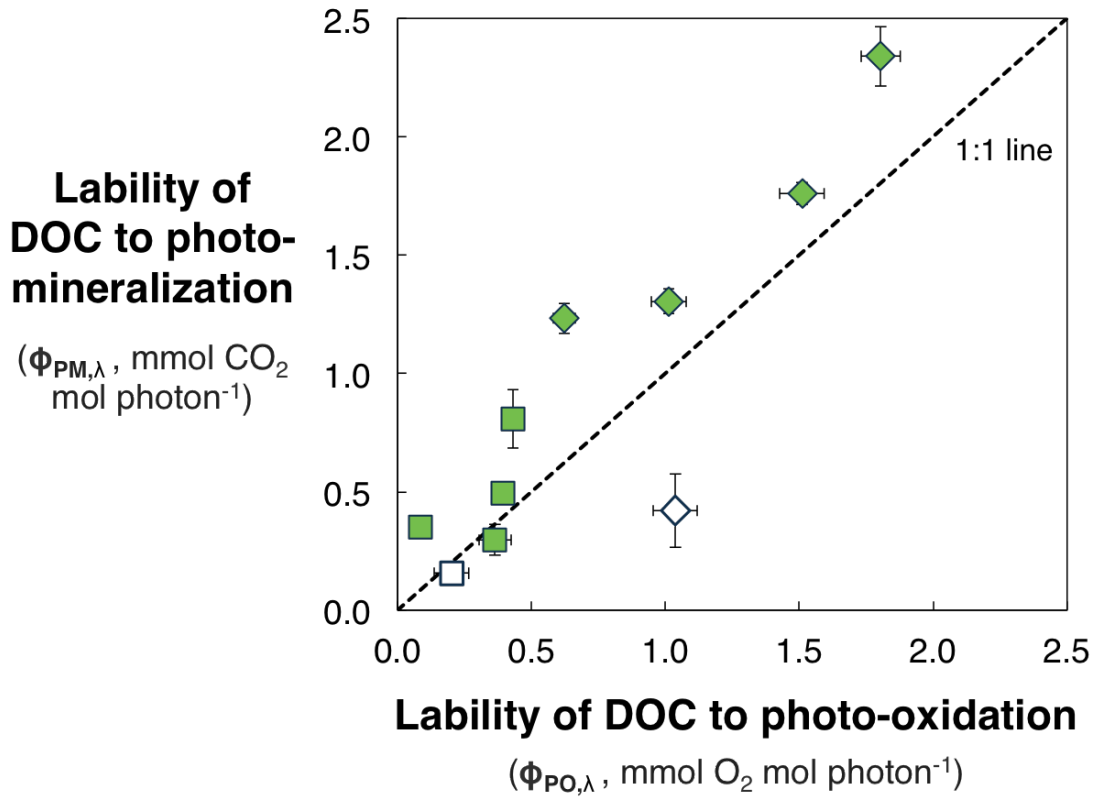

Figure S3. Apparent quantum yields for photomineralization and photo-oxidation of permafrost DOC. Apparent quantum yield (lability) for photomineralization ($\varphi_{PM,\lambda}$) versus the apparent quantum yield (lability) for photo-oxidation ($\varphi_{PO,\lambda}$) at UV (309 nm, diamond symbols) and visible (406 nm, square symbols) light plotted with the 1:1 line (dashed). Open symbols indicate the permafrost leachate with < 1 μM total dissolved iron. All values are shown as the average ± 1 standard error of experimental replicate vials (n = 4).

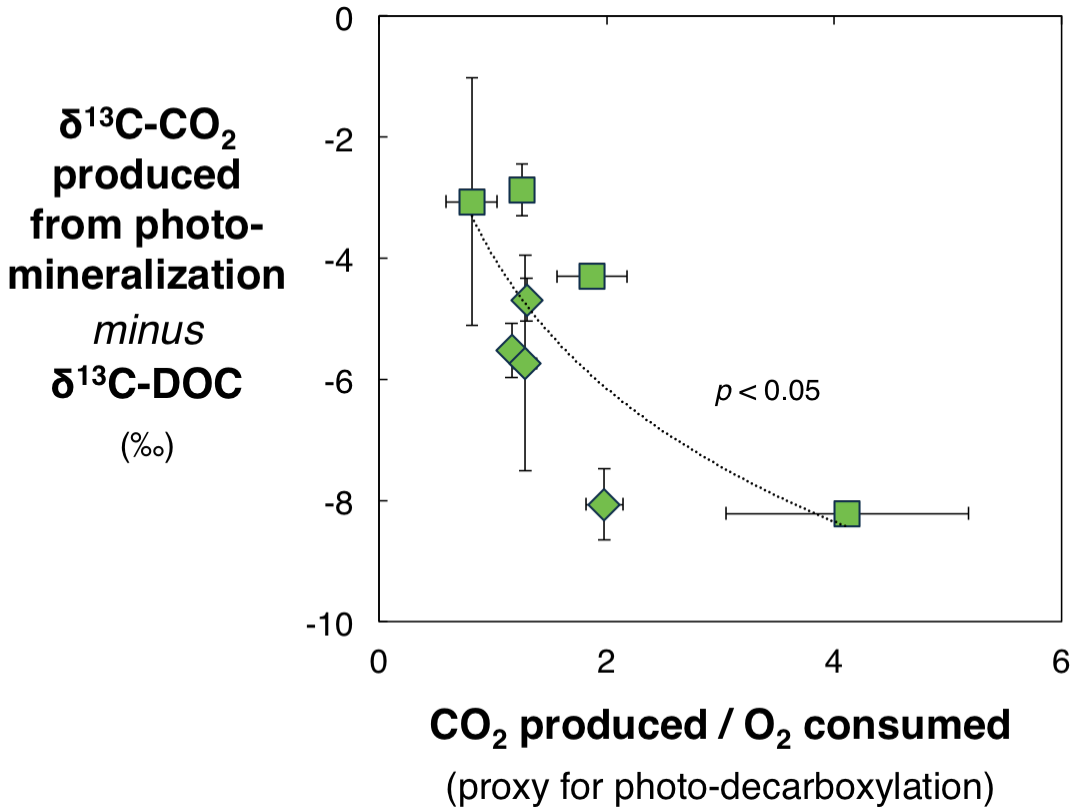

Figure S4. Photochemical production of ^{13}C-depleted CO_2 increased with the extent of photo-decarboxylation. δ^{13}C-CO_2 produced from photomineralization of permafrost DOC minus the δ^{13}C of initial, bulk DOC plotted versus the molar ratio of photochemical CO_2 production per O_2 consumed by permafrost DOC at UV (309 nm, diamond symbols) and visible (406 nm, square symbols) wavelengths of light. The molar ratio of photochemical CO_2 production to O_2 consumption is a proxy for the extent of photo-decarboxylation. Data were fit with a least-squares exponential model where $R^2 = 0.65$, t-statistic = 3.4, $p < 0.05$. Values on the x- and y-axes are shown as the average ± 1 standard error of experimental replicates (n = 4 and 2, respectively; see Methods).

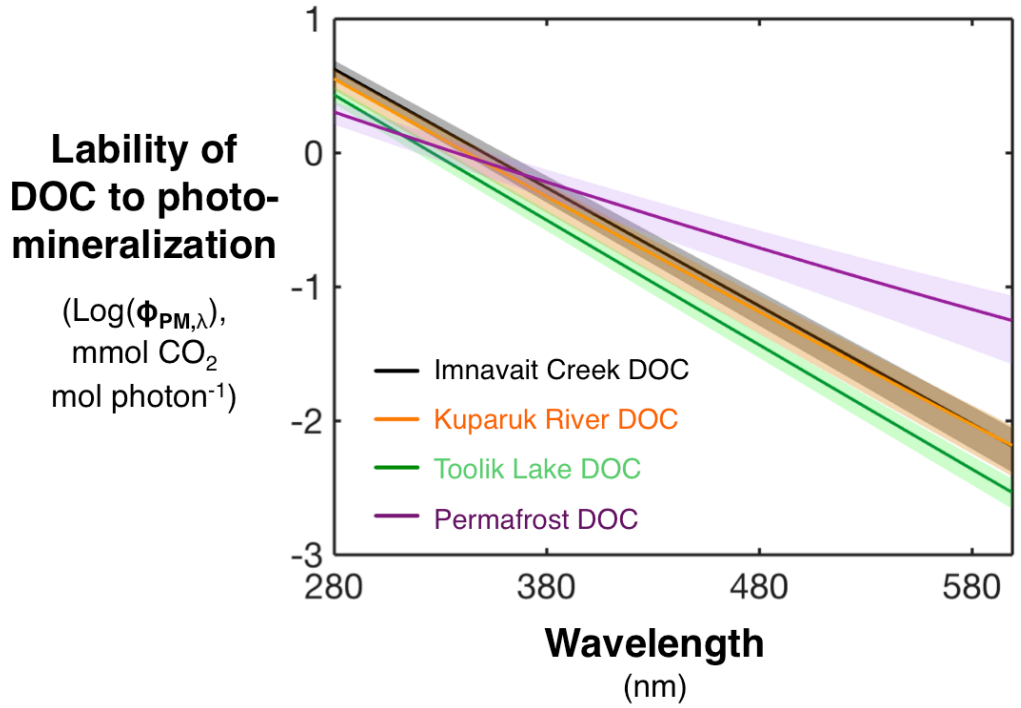

Figure S5. Photomineralization yield spectra for permafrost DOC were significantly shallower than for surface water DOC. Average wavelength-dependent apparent quantum yields (lability) for photomineralization ($\varphi_{PM,\lambda}$) of DOC in arctic surface waters compared to permafrost DOC measured in this study (Figure 1a). Data are plotted on the y-axis as $\log_{10}$ values of $\varphi_{PM,\lambda}$. Solid lines show the average $\varphi_{PM,\lambda}$ spectrum and the similar color shading shows the upper and lower 95% confidence intervals. $\varphi_{PM,\lambda}$ spectra were previously reported for DOC in Imnavait Creek, Kuparuk River, and Toolik Lake assuming an exponentially decaying spectrum (Cory et al., 2014). The $\varphi_{PM,\lambda}$ spectral slopes directly measured for permafrost DOC in this study (-0.005 ± 0.0004 $\log_{10}$(mmol CO_2) mol photon^{-1} nm^{-1}; average ± 1 SE; n = 5) were significantly shallower than those previously estimated indirectly for surface water DOC (-0.009 ± 0.0002 $\log_{10}$(mmol CO_2) mol photon^{-1} nm^{-1}; average ± 1 SE; n = 3; two-tailed, unpaired t-test; t-statistic = 7.4, $p < 0.001$).

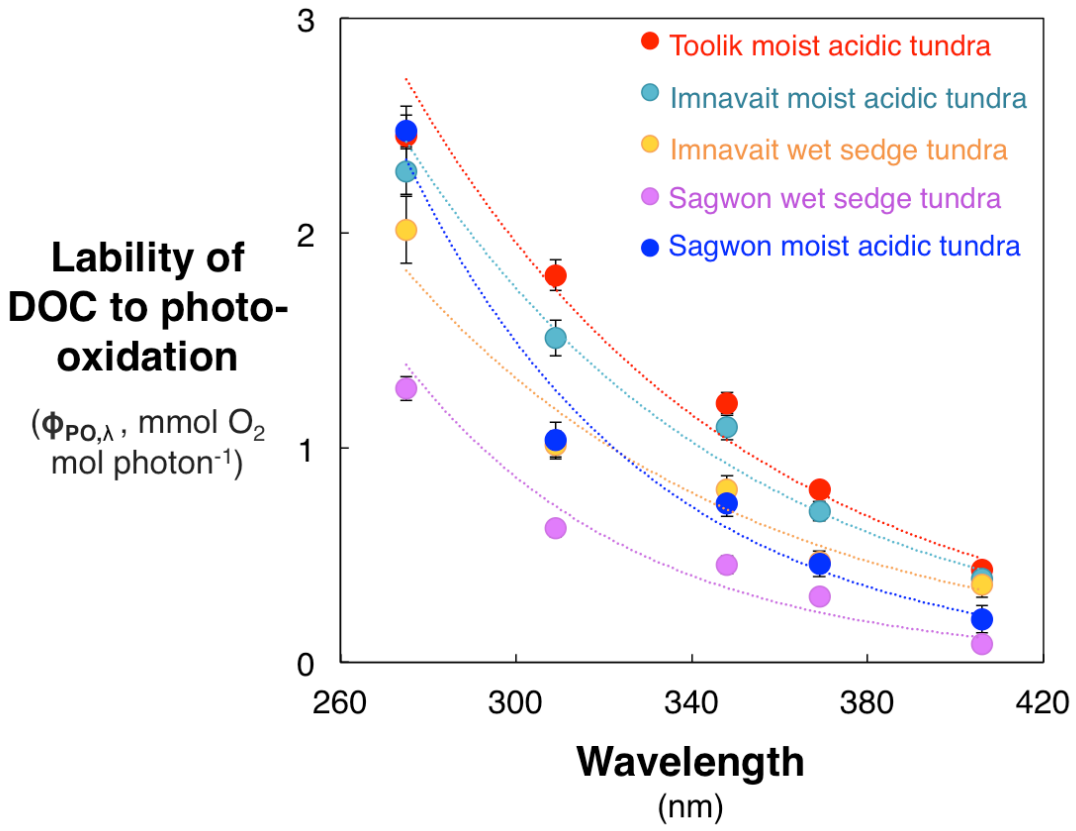

Figure S6. Wavelength-dependent apparent quantum yield (lability) for photo-oxidation ($\varphi_{PO,\lambda}$) of permafrost DOC. Each data series was fit to an exponential model using a least-squares regression where $R^2 > 0.93$, $p < 0.05$. All values are shown as the average ± 1 standard error of experimental replicate vials ($n = 4$).

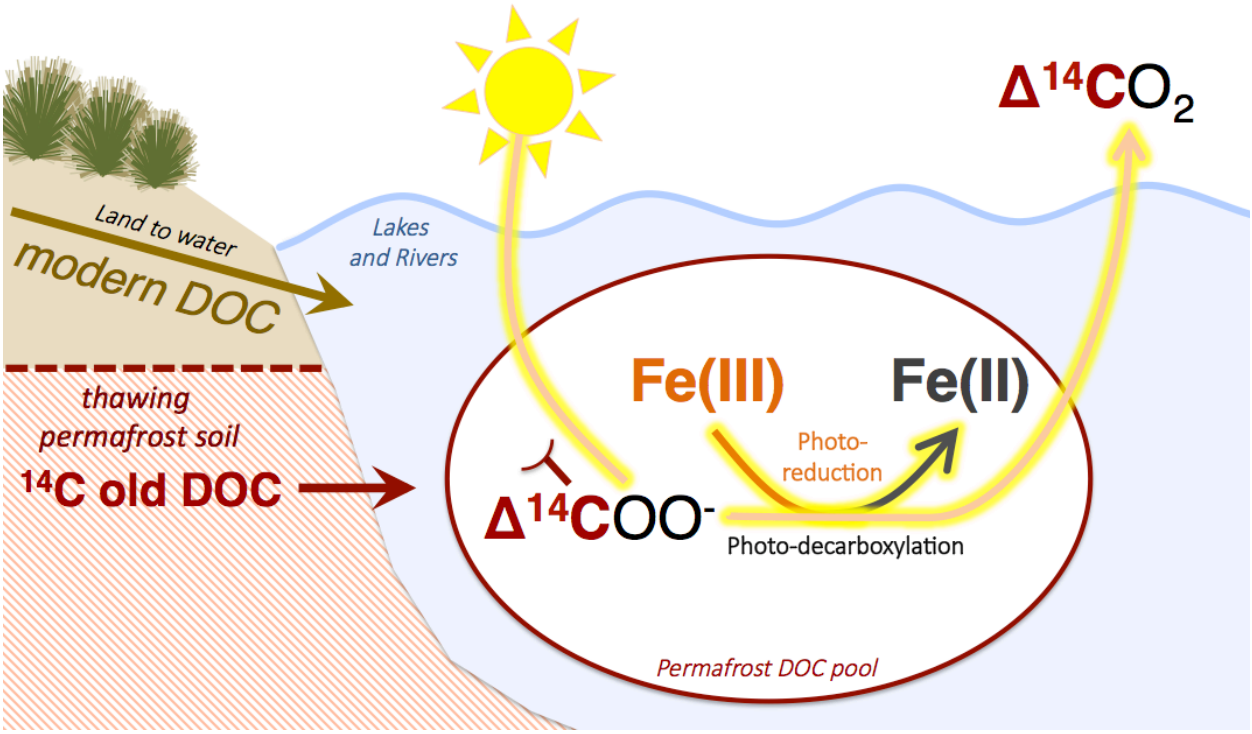

Figure S7. Sunlight and iron convert millennia-aged permafrost dissolved organic carbon to carbon dioxide in arctic surface water.

Table S1. Date, location, and depth of permafrost soil collection. Permafrost soils were collected on three glacial surfaces and from the two dominant vegetation types of the low Arctic (upland moist acidic tussock tundra and lowland wet sedge tundra; Mull & Adams, 1989; Walker et al., 2005; Hobbie & Kling, 2014). Thaw depth was not recorded during soil collection in 2015.

Permafrost soil	Landscape age (k a BP)	Glaciation	Date of soil collection	Latitude	Longitude	Depth of soil collection (cm)	Thaw depth (cm)
Toolik moist acidic tundra	14	Itkillik I	13 Jul 2015	68°37'46.97"N	149°34'49.29"W	95 – 110	--
			17 Jul 2018	68°37'16.18"N	149°36'54.17"W	75 – 90	24
Imnavait moist acidic tundra	250	Sagavanirktok	8 Jul 2013	68°36'51.86"N	149°18'30.87"W	90 – 105	20
			8 Jul 2013	68°36'51.86"N	149°18'30.87"W	90 – 105	17
			8 Jul 2013	68°36'51.86"N	149°18'30.87"W	90 – 105	21
			10 Jul 2018	68°36'35.36"N	149°18'29.80"W	70 – 85	15
Imnavait wet sedge tundra	250	Sagavanirktok	22 Jul 2015	68°36'33.89"N	149°18'52.58"W	90 – 130	--
			19 Jul 2018	68°36'31.90"N	149°18'47.90"W	100 – 130	50
Sagwon wet sedge tundra	> 2,500	Gunsight Mountain	20 Jul 2018	69°20'38.66"N	148°45'21.87"W	60 – 80	25
Sagwon moist acidic tundra	> 2,500	Gunsight Mountain	4 Aug 2015	69°25'28.70"N	148°41'39.05"W	90 – 100	--
			18 Jul 2018	69°20'36.81"N	148°45'31.75"W	75 – 90	40
Sagwon non-acidic tundra	> 2,500	Gunsight Mountain	4 Aug 2015	69°26'52.77"N	148°36'42.21"W	90 – 100	--

Table S2. Accession numbers for the permafrost leachates analyzed for carbon isotopes of DOC or DIC at the National Ocean Sciences Accelerator Mass Spectrometry facility. Permafrost leachates were prepared from soils collected in 2018 and the initial, bulk DOC was analyzed for ^{14}C and ^{13}C. DOC leached from the Toolik moist acidic tundra permafrost soil was analyzed in duplicate. Permafrost leachates were exposed to ≥ 100 mW narrow-banded (± 10 nm) LEDs at either 309 or 406 nm alongside one or two dark controls, and then the DIC in those waters was analyzed for ^{14}C and ^{13}C. Exposure of the Toolik moist acidic and Sagwon wet sedge tundra permafrost leachates to LEDs at 309 and 406 nm took place on separate days.

Accession #	Permafrost soil	DOC or DIC analyzed for ^{14}C and ^{13}C	Light exposure experiment #	Treatment
OS-146256	Sagwon wet sedge tundra	DOC	N/A	N/A
OS-146257	Sagwon moist acidic tundra	DOC	N/A	N/A
OS-147265	Toolik moist acidic tundra	DOC	N/A	N/A
OS-147266	Toolik moist acidic tundra	DOC	N/A	N/A
OS-147267	Imnavait moist acidic tundra	DOC	N/A	N/A
OS-147268	Imnavait wet sedge tundra	DOC	N/A	N/A
OS-147595	Toolik moist acidic tundra	DIC	1	Dark control
OS-147596	Toolik moist acidic tundra	DIC	1	Dark control
OS-147597	Toolik moist acidic tundra	DIC	1	LED-exposed, 309 nm
OS-147598	Imnavait moist acidic tundra	DIC	2	Dark control
OS-147599	Imnavait moist acidic tundra	DIC	2	Dark control
OS-147600	Imnavait moist acidic tundra	DIC	2	LED-exposed, 309 nm
OS-147601	Imnavait moist acidic tundra	DIC	2	LED-exposed, 406 nm
OS-147602	Imnavait wet sedge tundra	DIC	3	Dark control
OS-147603	Imnavait wet sedge tundra	DIC	3	Dark control
OS-147604	Imnavait wet sedge tundra	DIC	3	LED-exposed, 309 nm
OS-147605	Imnavait wet sedge tundra	DIC	3	LED-exposed, 406 nm
OS-147606	Sagwon wet sedge tundra	DIC	4	Dark control
OS-147607	Sagwon wet sedge tundra	DIC	4	Dark control
OS-147608	Sagwon wet sedge tundra	DIC	4	LED-exposed, 309 nm
OS-147655	Toolik moist acidic tundra	DIC	5	Dark control
OS-147656	Toolik moist acidic tundra	DIC	5	LED-exposed, 406 nm
OS-147941	Sagwon wet sedge tundra	DIC	6	Dark control
OS-147942	Sagwon wet sedge tundra	DIC	6	LED-exposed, 406 nm

Table S3. Summary of the light exposure time, photon dose, and amount of light absorbed by CDOM during the light exposure experiments to quantify photomineralization yields of permafrost DOC at 309 nm. DOC leached from permafrost soils was exposed to ≥ 100 mW, narrow-banded (± 10 nm) LEDs at 309 nm, simulated sunlight (Atlas Suntest XLS+), or natural sunlight. Details from the natural sunlight exposure of Imnavait moist acidic tundra permafrost DOC were previously reported (Ward & Cory, 2016). Light absorption by CDOM is reported as the average ± 1 standard error of replicate experiments with the permafrost leachates (n = 2, except Imnavait moist acidic tundra, which had n = 3).

Permafrost leachate	Light source	Light exposure time (hr)	Photon dose (mol photon m^{-2})	Light absorbed by CDOM (mol photon m^{-2})
Toolik moist acidic tundra	LED	12	2.42	2.35
	Suntest XLS+	18	73.3	7.46
Imnavait moist acidic tundra	LED	12	2.83	2.53
	Natural sunlight	16	52.0	0.87 ± 0.12
Imnavait wet sedge tundra	LED	12	2.70	2.52
	Suntest XLS+	18	73.3	5.03 ± 0.26
Sagwon wet sedge tundra	LED	12	2.66	2.38
Sagwon moist acidic tundra	LED	30	6.81	3.65
	Suntest XLS+	18	73.3	1.61 ± 0.11
Sagwon moist non-acidic tundra	Suntest XLS+	18	73.3	4.20 ± 0.12

Table S4. Concentrations, $\Delta^{14}C$, and $\delta^{13}C$ of DIC in the light-exposed and dark control permafrost leachates following exposure to ≥ 100 mW narrow-banded (± 10 nm) LEDs at 309 or 406 nm. Dark control water values are reported as the average ± 1 standard error of replicate flasks (*n* = 2). For the Imnavait moist acidic and wet sedge tundra permafrost leachates, the dark controls were the same for the LED exposures at 309 and 406 nm.

Permafrost leachate	LED wavelength (nm)	Light exposure time (hr)	DIC_{dark} (μM)	$\Delta^{14}C$-DIC_{dark} (‰)	$\delta^{13}C$-DIC_{dark} (‰)	DIC_{light} (μM)	$\Delta^{14}C$-DIC_{light} (‰)	$\delta^{13}C$-DIC_{light} (‰)
Toolik moist acidic tundra	309	8	61 ± 2	– 245 ± 1	– 6.0 ± 0.1	161	– 395	– 21.0
	406	10	41	– 189	– 9.6	113	– 391	– 22.5
Imnavait moist acidic tundra	309	14	45 ± 2	– 159 ± 2	– 9.8 ± 0.1	118	– 348	– 22.9
	406	14	45 ± 2	– 159 ± 2	– 9.8 ± 0.1	111	– 335	– 20.8
Imnavait wet sedge tundra	309	24	227 ± 4	– 406 ± 3	5.8 ± 0.1	325	– 448	– 5.4
	406	24	227 ± 4	– 406 ± 3	5.8 ± 0.1	307	– 440	– 3.2
Sagwon wet sedge tundra	309	20	177 ± 1	– 235 ± 1	– 1.0 ± 0.1	232	– 273	– 9.1
	406	24.6	225	– 176	– 2.0	272	– 216	– 8.0

Table S5. Total summertime UV and visible photon doses at the Toolik Lake Field Station from 15 May to 1 October for 2012, 2015, 2016, and 2017.

	Total summertime photon dose (mol photon m^{-2})	
Year	UV 280 – 400 nm	Visible 401 – 700 nm
2012	359	3,501
2015	365	3,907
2016	289	2,839
2017	566	7,062

Table S6. Leaching conditions and chemical attributes of the permafrost leachates prepared from soils collected in 2018. Two different permafrost leachates were prepared from each permafrost soil to achieve objectives (i) and (ii) of this study (see Supporting Methods). The exception was Sagwon moist acidic tundra permafrost soil, which was not used for study objective (ii).

Objective:	(i) Characterize the photomineralization yield spectra for permafrost DOC					(ii) Quantify the ^{14}C and ^{13}C compositions of CO_2 produced by sunlight			
	Toolik moist acidic tundra	Imnavait moist acidic tundra	Imnavait wet sedge tundra	Sagwon wet sedge tundra	Sagwon moist acidic tundra	Toolik moist acidic tundra	Imnavait moist acidic tundra	Imnavait wet sedge tundra	Sagwon wet sedge tundra
Frozen soil weight (g)	800	812	803	800	803	2,292	3,261	1,448	2,391
Thaw time (hr)	13	12.5	18	13	12.5	12.5	12.5	19.5	12.5
DOC leaching rate (μmol C g-soil^{-1} d^{-1})	15.2	3.9	9.4	6.4	4.6	12.7	2.1	10.5	4.1
pH	6.5	5.8	7.0	6.5	8.0	5.8	6.0	7.0	7.2
Specific conductivity (μS cm^{-1})	17	9	28	18	146	29	12	51	34
Total Fe[a] (μM)	15.7	9.8	4.7	1.9	ND	30.0	31.0	8.8	1.7
Fe(II)[a] (μM)	8.4	5.6	ND	ND	ND	17.6	23.7	1.3	ND
Total Fe[b] (μM)	17.3	11.6	4.8	1.4	0.2	31.8	32.2	9.7	2.1
Total Mn[b] (μM)	0.3	0.1	0.1	0.5	0.4	0.7	0.3	0.2	0.8
DOC (μM)	2,435	643	1,520	1,019	718	5,820	1,340	3,017	1,931
a_{305} (m^{-1})	39	21	30	24	10	70	46	52	42
$SUVA_{254}$ (L mg^{-1} C m^{-1})	1.13	2.17	1.47	1.63	1.16	0.87	2.28	1.25	1.56
S_R (unitless)	0.87	0.92	1.09	0.94	1.00	0.88	0.81	0.94	0.93
Fluorescence index (unitless)	1.68	1.49	1.63	1.58	1.73	1.73	1.61	1.63	1.72

[a]Quantified using the colorometric Ferrozine method (Stookey, 1970).
[b]Quantified using inductively coupled plasma mass spectrometry (Linge & Jarvis, 2009).

Table S7. Chemical attributes of permafrost leachates prepared from soils collected in 2013 and 2015. All values are reported as the average ± 1 standard error of replicate experiments (n = 2, except Imnavait moist acidic tundra, which had n = 3, and Toolik moist acidic tundra, which did not have an experimental replicate). The pH, specific conductivity, DOC, and $SUVA_{254}$ for these permafrost leachates were previously reported (Ward & Cory, 2015; Ward et al., 2017). Dissolved Fe(II) was not measured for the Imnavait moist acidic tundra permafrost leachate (Ward & Cory, 2015). ND = not detectable.

	Toolik moist acidic tundra	Imnavait moist acidic tundra	Imnavait wet sedge tundra	Sagwon moist acidic tundra	Sagwon moist non-acidic tundra
pH	7.0	5.8 ± 0.1	5.5 ± 0.1	7.7 ± 0.1	7.3 ± 0.1
Specific conductivity ($\mu S\ cm^{-1}$)	30	9 ± 1	15 ± 1	177 ± 1	133 ± 3
Total Fe (μM)	37.8	23.1 ± 0.9	10.1 ± 0.1	ND	2.6 ± 0.2
Fe(II) (μM)	20.8	--	3.2 ± 0.5	ND	ND
DOC (μM)	2,356	998 ± 18	1,595 ± 20	2,077 ± 29	1,550 ± 68
a_{305} (m^{-1})	66	17 ± 3	55 ± 3	32 ± 1	63 ± 1
$SUVA_{254}$ ($L\ mg^{-1}\ C\ m^{-1}$)	1.92	1.23 ± 0.15	2.27 ± 0.07	1.32 ± 0.01	2.91 ± 0.12
S_R (unitless)	0.85	0.96 ± 0.04	0.85 ± 0.01	0.88 ± 0.01	0.96 ± 0.1
Fluorescence index (unitless)	1.66	1.55 ± 0.01	1.53 ± 0.01	1.79 ± 0.01	1.61 ± 0.01
Aromatic C (%)	13	12	19 ± 1	11 ± 1	21 ± 1
Carboxyl C (%)	11	15	11 ± 1	12 ± 1	14 ± 1

References Cited

Benner, R., Fogel, M. L., Sprague, E. K., & Hodson, R. E. (1987). Depletion of ^{13}C in lignin and its implications for stable carbon isotope studies. *Nature* 329, 708-710. https://doi.org/10.1038/329708a0

Bertoldi, D., Santato, A., Paolini, M., Barbero, A., Camin, F., Nicolini, G., & Larcher, R. (2014). Botanical traceability of commercial tannins using the mineral profile and stable isotopes. *J. Mass Spectrom.* 49, 792-801. https://doi.org/10.1002/jms.3457

Cooley, S. W., Smith, L. C., Ryan, J. C., Pitcher, L. H., & Pavelsky, T. M. (2019). Arctic-Boreal lake dynamics revealed using CubeSat imagery. *Geophysical Research Letters* 46, 2111–2120. https://doi.org/10.1029/2018GL081584

Cory, R. M., Crump, B. C., Dobkowski, J. A., & Kling, G. W. (2013). Surface exposure to sunlight stimulates CO_2 release from permafrost soil carbon in the Arctic. *Proc. Natl. Acad. Sci. USA* 110, 3429-3434. https://doi.org/10.1073/pnas.1214104110

Cory, R. M., Harrold, K. H., Neilson, B. T., & Kling, G. W. (2015). Controls on dissolved organic matter (DOM) degradation in a headwater stream: the influence of photochemical and hydrological conditions in determining light-limitation or substrate-limitation of photo-degradation. *Biogeosciences* 12, 6669-6685. https://doi.org/10.5194/bg-12-6669-2015

Cory, R. M., McKnight, D. M., Chin, Y. -P., Miller, P., & Jaros, C. L. (2007). Chemical characteristics of fulvic acids from Arctic surface waters: Microbial contributions and photochemical transformations. *J. Geophys. Res.* 112, G04S51. https://doi.org/10.1029/2006JG000343

Cory, R. M., Ward, C. P., Crump, B. C., & Kling, G. W. (2014). Sunlight controls water column processing of carbon in arctic fresh waters. *Science* 345, 925-928. https://doi.org/10.1126/science.1253119

Fujii, M., Imaoka, A., Yoshimura, C., & Waite, T. D. (2014). Effects of molecular composition of natural organic matter on ferric iron complexation at circumneutral pH. *Environ. Sci. Technol.* 48, 4414-4424. https://doi.org/10.1021/es405496b

Hobbie, J. E., & Kling, G. W. (Eds.). (2014). *Alaska's Changing Arctic: Ecological Consequences for Tundra, Streams, and Lakes.* Oxford, UK: Oxford University Press.

Jankowski, J. J., Kieber, D. J., & Mopper, K. (1999). Nitrate and nitrite ultraviolet actinometers. *Photochem. Photobiol. Sci.* 70(3), 319-328. https://doi.org/10.1111/j.1751-1097.1999.tb08143.x

Judd, K. E., & Kling, G. W. (2002). Production and export of dissolved C in arctic tundra mesocosms: the roles of vegetation and water flow. *Biogeochemistry* 60, 213-234. https://doi.org/10.1023/A:1020371412061

Kling, G. W., Adams, H. E., Bettez, N. D., Bowden, W. B., Crump, B. C., Giblin, A. E., et al. (2014). Land-Water Interactions. In J. E. Hobbie & G. W. Kling (Eds.), *Alaska's Changing Arctic: Ecological Consequences for Tundra, Streams, and Lakes* (pp. 143–172). Oxford, UK: Oxford University Press.

Kling, G. W., Kipphut, G. W., & Miller, M. C. (1991). Arctic Lakes and Streams as Gas Conduits to the Atmosphere: Implications for Tundra Carbon Budgets. Science 251, 298-301. https://doi.org/10.1126/science.251.4991.298

Kling, G. W., Kipphut, G. W., Miller, M. M., & O'Brien, J. W. (2000). Integration of lakes and streams in a landscape perspective: the importance of material processing on spatial patterns and temporal coherence. Freshw. Biol. 43, 477–497. https://doi.org/10.1046/j.1365-2427.2000.00515.x

Li, A., Aubeneau, A. F., King, T., Cory, R. M., Neilson, B. T., Bolster, D., & Packman, A. I. (2019). Effects of vertical hydrodynamic mixing on photomineralization of dissolved organic carbon in arctic surface waters. *Environ. Sci.: Processes Impacts* 21, 748-760. https://doi.org/10.1039/c8em00455b

Linge, K. L., & Jarvis, K. E. (2009). Quadrupole ICP-MS: Introduction to instrumentation, measurement techniques and analytical capabilities. *Geostand, Geoanal. Res.* 33(4), 445-467. https://doi.org/10.1111/j.1751-908X.2009.00039.x

McGuire, A. D., Anderson, L. G., Christensen, T. R., Dallimore, S., Guo, L., Hayes, D. J., et al. (2009). Sensitivity of the carbon cycle in the Arctic to climate change. *Ecological Monographs* 79, 523-555. https://doi.org/10.1890/08-2025.1

McGuire, A. D., Lawrence, D. M., Koven, C., Clein, J. S., Burke, E., Chen, G., et al. (2018). Dependence of the evolution of carbon dynamics in the northern permafrost region on the trajectory of climate change. *Proc. Natl. Acad. Sci. USA* 115, 3882-3887. https://doi.org/10.1073/pnas.1719903115

Merck, M. F., Neilson, B. T., Cory, R. M., & Kling, G. W. (2012). Variability of in-stream and riparian storage in a beaded arctic stream. *Hydrol. Process*. 26, 2938–2950. https://doi.org/10.1002/hyp.8323

Miller, W. L., & Zepp, R. G. (1995). Photochemical production of dissolved inorganic carbon from terrestrial organic matter: Significance to the oceanic organic carbon cycle. *Geophys. Res. Lett.* 22, 417-420. https://doi.org/10.1029/94GL03344

Mull, C. G., & Adams, K. E. (Eds.). (1989). *Bedrock Geology of the Eastern Koyukuk Basin, Central Brooks Range, and Eastcentral Arctic Slope Along the Dalton Highway, Yukon River to Prudhoe Bay, Alaska* (guidebook 7, vol. 1). Anchorage, AK: Department of Natural Resources, Division of Geological and Geophysical Surveys.

Neilson, B. T., Cardenas, M. B., O'Connor, M. T., Rasmussen, M. T., King, T. V., & Kling, G. W. (2018). Groundwater flow and exchange across the land surface explain carbon export patterns in continuous permafrost watersheds. *Geophys. Res. Lett.* 45, 7596–7605. https://doi.org/10.1029/2018GL078140

Ping, C. L., Bockheim, J. G., Kimble, J. M., Michaelson, G. J., & Walker, D. A. (1998). Characteristics of cryogenic soils along a latitudinal transect in Arctic Alaska. *J. Geophys. Res.* 103, 28917–28928. https://doi.org/10.1029/98JD02024

Plaza, C., Pegoraro, E., Bracho, R., Celis, G., Crummer, K. G., Hutchings, J. A., et al. (2019). Direct observation of permafrost degradation and rapid soil carbon loss in tundra. *Nat. Geosci.* 12, 627-631. https://doi.org/10.1038/s41561-019-0387-6

Ratti, M., Canonica, S., McNeill, K., Erickson, P. R., Bolotin, J., & Hofstetter, T. B. (2015). Isotope fractionation associated with the direct photolysis of 4-chloroaniline. *Environ. Sci. Technol.* 49(7), 4263–4273. https://doi.org/10.1021/es505784a

Šmejkalová, T., Edwards, M. E., & Dash, J. (2016). Arctic lakes show strong decadal trends in earlier spring ice-out. *Nature Sci. Reports,* 6, 38449. https://doi.org/10.1038/srep38449

Stookey, L. L. (1970). Ferrozine—A new spectrophotometric reagent for iron. *Anal. Chem.* 42, 779–781. https://doi.org/10.1021/ac60289a016

Trusiak, A., Treibergs, L. A., Kling, G. W., & Cory, R. M. (2019). The controls of iron and oxygen on hydroxyl radical (•OH) production in soils. *Soil Syst.* 3, 1. https://doi.org/10.3390/soilsystems3010001

Turetsky, M. R., Abbott, B. W., Jones, M. C., Anthony, K. W., Olefeldt, D., Schuur, E. A. G., et al. (2019). Permafrost collapse is accelerating carbon release. *Nature* 569, 32-34. https://doi.org/10.1038/d41586-019-01313-4

Walker, D. A., Raynolds, M. K., Daniëls, F. J. A., Einarsson, E., Elvebakk, A., Gould, W. A., et al. (2005). The Circumpolar Arctic vegetation map. *J. Veg. Sci.* 16, 267-282. https://doi.org/10.1111/j.1654-1103.2005.tb02365.x

Ward, C. P., & Cory, R. M. (2015). Chemical composition of dissolved organic matter draining permafrost soils. *Geochim. Cosmochim. Acta* 167, 63-79. https://doi.org/10.1016/j.gca.2015.07.001

Ward, C. P., & Cory, R. M. (2016). Complete and partial photo-oxidation of dissolved organic matter draining permafrost soils. *Environ. Sci. Technol.* 50, 3545-3553. https://doi.org/10.1021/acs.est.5b05354

Ward, C. P., Nalven, S. G., Crump, B. C., Kling, G. W., & Cory, R. M. (2017). Photochemical alteration of organic carbon draining permafrost soils shifts microbial metabolic pathways and stimulates respiration. *Nat. Commun.* 8(722), 1-8. https://doi.org/10.1038/s41467-017-00759-2

Willach, S., Lutze, H. V., Eckey, K., Löppenberg, K., Lüling, M., Wolbert, J. B., et al. (2018). Direct photolysis of sulfamethoxazole using various irradiation sources and wavelength ranges - Insights from degradation product analysis and compound-specific stable isotope analysis. *Environ. Sci. Technol.* 52(3), 1225–1233. https://doi.org/10.1021/acs.est.7b04744

Xie, H., Zafiriou, O. C., Cai, W. -J., Zepp, R. G., & Wang, Y. (2004). Photooxidation and its effects on the carboxyl content of dissolved organic matter in two coastal rivers in the southeastern United States. *Environ. Sci. Technol.* 38(15), 4113−4119. https://doi.org/10.1021/es035407t